

Studying phonon coherence with a quantum sensor

Agnetta Y. Cleland, E. Alex Wollack, and Amir H. Safavi-Naeini*
Department of Applied Physics and Ginzton Laboratory, Stanford University
348 Via Pueblo Mall, Stanford, California 94305, USA
(Dated: February 2, 2023)

In the field of quantum technology, nanomechanical oscillators offer a host of useful properties given their compact size, long lifetimes, and ability to detect force and motion. Their integration with superconducting quantum circuits shows promise for hardware-efficient computation architectures and error-correction protocols based on superpositions of mechanical coherent states. One limitation of this approach is decoherence processes affecting the mechanical oscillator. Of particular interest are two-level system (TLS) defects in the resonator host material, which have been widely studied in the classical domain, primarily via measurements of the material loss tangent. In this manuscript, we use a superconducting qubit as a quantum sensor to perform phonon number-resolved measurements on a phononic crystal cavity. This enables a high-resolution study of mechanical dissipation and dephasing in coherent states of variable size (mean phonon number $\bar{n} \simeq 1 - 10$). We observe nonexponential energy decay and a state size-dependent reduction of the dephasing rate, which we attribute to interactions with TLS. Using a numerical model, we reproduce the energy decay signatures (and to a lesser extent, the dephasing signatures) via mechanical emission into a small ensemble ($N = 5$) of saturable and rapidly dephasing TLS. Our findings comprise a detailed examination of TLS-induced phonon decoherence in the quantum regime.

INTRODUCTION

Nanomechanical oscillators hold the potential to serve as long-lived memories for computation [1, 2], transducers for communication [3–5], and high-precision quantum sensors [6]. Their ability to interact with superconducting qubits through the piezoelectric effect has allowed mechanical systems to be brought into the quantum regime [7–16]. In order to fully realize the potential of this hybrid platform, it is crucial to understand decoherence processes affecting mechanical oscillators in the quantum limit. For mechanical states with large numbers of phonons ($\bar{n} \gg 1$), the established work has followed semiclassical spectroscopic methods to detect time-averaged energy loss [17–19] and frequency noise [20, 21] in the resonator. More recent studies of mechanical devices in the few-phonon regime have used a superconducting qubit to perform single-phonon characterization [8, 10, 16, 22]. In this manuscript, we use a Ramsey protocol with a superconducting qubit that allows us to perform time- and phonon number-resolved measurements on a mechanical resonator [22, 23]. This technique, which could easily be extended to other bosonic systems, affords us a highly granular picture of how larger mechanical states of an oscillator evolve in time, shedding new light on the quantum nonlinear dissipation processes.

The mechanical dissipation dynamics we observe are consistent with emission into a bath of rapidly dephasing two-level system (TLS) defects, similar to those which exist in amorphous glasses and imperfect crystalline materials [24]. TLS can couple to electromagnetic and elastic fields, creating a dissipation channel for nearby modes

[25–27]. The dynamics of TLS-induced decay and decoherence at microwave frequencies have been the subject of extensive study in both electromagnetic [20, 28–31] and nanomechanical systems [17–19, 32–34]. Their contribution to microwave loss has been shown to depend on power and temperature, allowing the TLS-induced loss tangent to be extracted from measurements of the resonator’s frequency and quality factor [19, 28]. In particular, TLS contribution to dielectric loss is known to be saturable – it is suppressed when the intra-cavity energy exceeds a critical threshold. In this regime, the TLS spontaneous excitation and emission rates equilibrate as the TLS reach a steady state in which they no longer absorb energy from the resonator mode. Prior studies of TLS saturation have involved monitoring the scattered response of a resonator for a range of drive powers [19, 28, 29]. In this work, the qubit nonlinearity allows for quantum non-demolition measurement of the mechanical state via established circuit QED techniques. We leverage this approach to observe signatures of TLS-induced dissipation in the time domain, which we reproduce using a simple numerical model.

DEVICE DESCRIPTION

The mechanical oscillators under study are one-dimensional phononic crystal cavities made of thin-film lithium niobate (LN). While the device contains two resonators, these experiments focus on only one cavity, which supports the higher frequency mode (Fig 1a). The cavity is formed from periodic structures, acting as acoustic mirrors, which support a defect site from both ends [35]. The periodicity of the mirrors gives rise to a full phononic bandgap which protects the localized mode from phonon radiation channels (supplementary Fig. S1

* safavi@stanford.edu

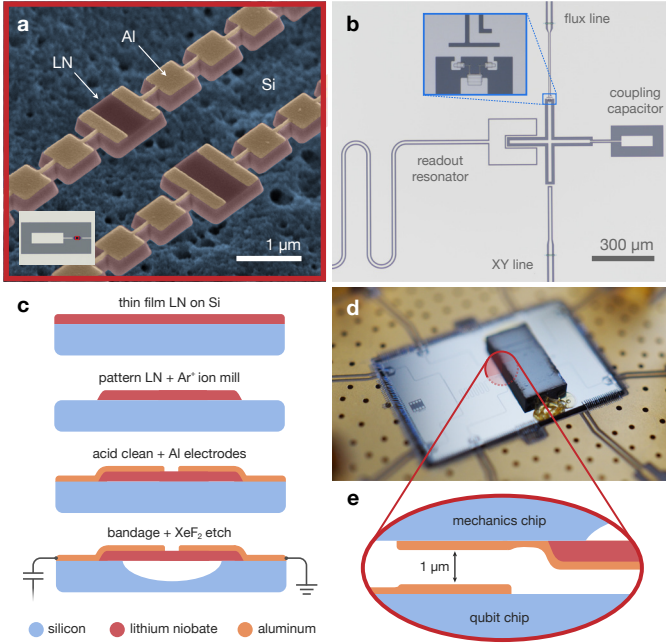


FIG. 1. **Device and fabrication.** **a**, False-color scanning electron micrograph of the mechanical resonators. Lithium niobate phononic crystal cavities (red) are patterned with aluminum electrodes (orange) and undercut from the silicon substrate (blue). Inset shows an optical micrograph of the coupling capacitor pad, which is galvanically connected to the mechanical electrodes. The resonators are too small to be seen in this image, but their location is indicated in red. **b**, Optical micrograph of the bottom chip, showing the superconducting qubit, control lines, and readout resonator. Inset shows the qubit's SQUID and flux line. **c**, Mechanical device fabrication. Cross-sectional illustration of the patterning, cleaning, metallization, and release etching steps. Bandages create electrical contact between the active mechanics electrode and the coupling capacitor pad, as well as between the ground electrode and the chip's ground plane. **d**, Photograph of the composite flip-chip assembly. Control lines on the qubit (bottom) chip are visible, as well as the polymer adhesive which fixes the top chip in place. **e**, Approximate location of the cross-chip coupling capacitor. The illustration shows the two halves of the coupling capacitor (orange) aligned vertically and separated by approximately 1 μm .

and Section I). This design approach, and the large coupling strengths arising from the strong piezoelectric effect of LN, make these devices a compelling platform for studies in quantum acoustics, because it robustly removes the effects of clamping and other linear scattering losses. Furthermore, the small mode volume of these cavities make them an ideal candidate for studies of TLS as mechanical loss channels, since it yields stronger coupling to fewer TLS.

We assemble our device in a hybrid flip-chip architecture. The mechanical resonators are fabricated on the top chip, and the bottom chip includes a superconducting qubit, control lines, and a coplanar waveguide readout resonator (Fig. 1b). The qubit is a frequency-tunable

planar transmon, with an on-chip flux line providing capability for both static and pulsed frequency control (Fig 1b, inset). The qubit fabrication is described in prior work [11, 16] and follows methods developed in Ref. [36]. As illustrated in Fig. 1c, the mechanics fabrication process begins with thin-film LN on a silicon substrate. We thermally anneal the sample for 8 hours at 500 C before thinning the LN by argon ion milling to a target final thickness of 250 nm. The nanomechanical structures are then patterned by electron-beam lithography and argon ion milling using a hydrogen silesquioxane (HSQ) mask. We remove redeposited material from the LN sidewalls in a heated bath of dilute hydrofluoric acid, followed by a piranha etch. Next, we define metallic layers with a combination of electron-beam and photolithography, including bandages to create the relevant galvanic connections. We perform an oxygen plasma descum before each deposition to minimize the presence of polymer residues at metallic interfaces. Finally, we undercut the nanomechanical structures from the substrate with a masked xenon difluoride (XeF₂) dry etch. This concludes the mechanical device fabrication, before the LN chip is aligned and bonded to an accompanying qubit chip (Fig. 1d) in a submicron die bonder [16, 37]. The qubit is capacitively coupled to the mechanical mode across a small vacuum gap, which is defined by the flip-chip separation distance (Fig. 1e).

The completed flip-chip package is cooled to a temperature of 10 mK in a dilution refrigerator. As we bias the qubit away from its maximum frequency $\omega_{\text{ge}}^{\text{max}}/2\pi = 2.443$ GHz, we measure the qubit T_1 over a wide tuning range to find a mean value $T_1 = 4.9 \pm 2.3 \mu\text{s}$, with $T_2 = 1.4 \mu\text{s}$ at the flux sweet spot. When the qubit is rapidly tuned into resonance with the mechanics at $\omega_{\text{m}}/2\pi = 2.339$ GHz, the resulting Rabi oscillations allow us to extract the coupling rate $g/2\pi = 10.5 \pm 0.1$ MHz. Further details on basic device characterization can be found in a prior manuscript [16].

PHONON NUMBER MEASUREMENTS

In the following experiments, we statically bias the qubit near the mechanical mode and use it as a probe to study dissipation and dephasing of mechanical coherent states. We extract information about the mechanical state through the qubit spectrum by means of their dispersive coupling. The qubit and mechanics are coupled through the piezoelectric effect to give an interaction Hamiltonian $\hat{H}_{\text{int}} = g(\hat{b} + \hat{b}^\dagger)\hat{\sigma}_x$, with \hat{b} corresponding to the mechanics and Pauli operators $\hat{\sigma}$ corresponding to the qubit. When the two modes are far detuned, the effective Hamiltonian for the system is given by [38]:

$$\hat{H}_{\text{eff}} = \omega_{\text{m}}\hat{b}^\dagger\hat{b} + \frac{1}{2}\left(\omega_{\text{ge}} + 2\chi\hat{b}^\dagger\hat{b}\right)\hat{\sigma}_z.$$

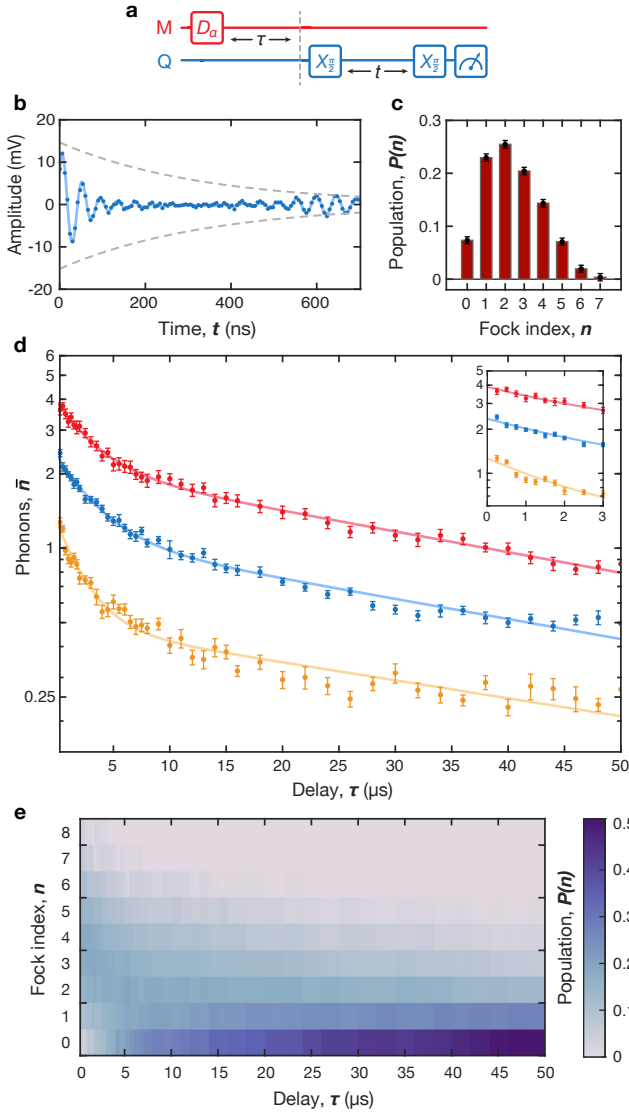


FIG. 2. **Energy decay measurement.** **a**, Pulse sequence showing a displacement \hat{D}_α which prepares a mechanical coherent state (left) and mechanical state readout using a Ramsey measurement (right) after a variable delay τ . The Ramsey measurement consists of two $\pi/2$ rotations of the qubit state, separated by a variable delay t . **b**, Representative time domain trace from a Ramsey measurement. The data (points) and a fit to Eq. 1 (solid line) are shown, along with the fitted exponential decay envelope (dashed line). **c**, Phonon number distribution extracted from the time domain data in **b**. All error bars represent one standard deviation. **d**, Sample ringdown measurements with varied initial state sizes. Inset shows an expanded view of the early-time data, $\tau \leq 3 \mu\text{s}$. **e**, Evolution of phonon number distribution for an initial state size $\bar{n}_0 = 3.89$ (red data set in **d**). The color plot indicates the population in each Fock level at each point in time.

In this limit, the qubit spectrum acquires a frequency shift 2χ for each populated energy level in the mechanical oscillator. The magnitude of this shift depends on the qubit anharmonicity α_q , mechanical coupling rate g , and

detuning $\Delta = \omega_{\text{ge}} - \omega_{\text{m}}$ as:

$$\chi = -\frac{g^2}{\Delta} \frac{\alpha_q}{\Delta - \alpha_q}.$$

Since this value varies with the qubit frequency, it is important to choose an operating point which yields a large χ while keeping the system in the strong dispersive limit. In this regime, χ exceeds all decoherence rates of the system, but the detuning is sufficiently large to prevent significant linear coupling between the two modes. For our experiments, we statically bias the qubit to $\omega_{\text{ge}}/2\pi = 2.262 \text{ GHz}$, which corresponds to $|\Delta| \approx 8g$ and a measured dispersive shift $2\chi/2\pi = -1.48 \pm 0.05 \text{ MHz}$.

When the mechanical mode is populated, we can perform a Ramsey measurement on the qubit to resolve the array of dispersive shifts and thus obtain the full phonon number distribution of the mechanical state. The Ramsey signal $S(t)$ takes the form of a sum of oscillating terms whose frequencies differ by integer multiples of 2χ , indexed by the Fock number n , with an exponentially decaying envelope:

$$S(t) = \sum_{n=0}^{n_{\text{max}}} A_n e^{-\kappa t} \cos\left((\omega_0 + 2\chi n)t + \varphi_n\right). \quad (1)$$

We fit the Ramsey signal to Eq. 1 with fit parameters A_n , κ , and χ . We extract the phonon number distribution from the normalized amplitudes, $P(n) = A_n / \sum_n A_n$. In contrast to previous work [16] where the exponential decay rate in Eq. 1 was taken to depend linearly on n , we choose here to model decay as independent of the phonon occupation number (supplementary Section II).

PHONON-RESOLVED DECAY

We use the Ramsey protocol to study decay of mechanical coherent states. We first apply a displacement pulse \hat{D}_α at the mechanical frequency to the qubit's XY line (Fig. 2a), which drives the mechanics into a coherent state. After a variable delay τ , we perform a Ramsey measurement on the qubit to extract the mechanical $P(n)$, as described above (Fig. 2b,c). From this, we calculate the average number of phonons, $\bar{n} = \sum_{n=0} n \cdot P(n)$. Repeating this sequence for a range of τ values constitutes a *phonon-number resolved* ringdown measurement of a mechanical coherent state (Fig. 2d). The measurement provides a high degree of resolution, revealing not only the decaying mean phonon number in the resonator, but also how the distribution evolves in time (Fig. 2e and Fig. S2).

We observe that the mechanical dissipation follows a double-exponential trajectory, with an initial fast decay followed by significantly slower relaxation. Similar multi-exponential behavior appears in single-phonon measurements in a prior study of the same device [16]. By varying

the duration and amplitude of the initial displacement pulse, we study how the energy decay and saturation dynamics depend on the size of the initial mechanical state (Fig. 2d). We fit each decay curve to a double-exponential form:

$$\bar{n}(\tau) = a_1 e^{-\kappa_1 \tau} + a_2 e^{-\kappa_2 \tau}. \quad (2)$$

We examine the behavior of the fast decay $\kappa_1/2\pi \simeq 30 - 70$ kHz, slow decay $\kappa_2/2\pi \simeq 1 - 3$ kHz, and their corresponding weights a_1, a_2 as we vary the initial mean phonon number \bar{n}_0 .

Nonexponential decay has been observed in superconducting qubits due to fluctuations in quasiparticle population [39] as well as in graphene mechanical resonators operated in a strongly nonlinear regime [40]. Neither mechanism is plausible in our experiments. We argue that the multi-exponential energy decay in our system is caused by resonant interaction of the mechanics with a handful of rapidly dephasing TLS. The initial fast decay occurs as the mechanical mode emits energy into the TLS. We note that we do not observe any coherent oscillations between the two coupled systems. As the TLS become populated, they lose their ability to absorb more phonons, thus becoming saturated. Consequently, the rapid decay ends and slower decay emerges, caused by either energy relaxation of the TLS or other dissipation processes affecting the resonator. We perform numerical modeling to reproduce the salient features of this process, described later in this paper.

PHONON-RESOLVED DEPHASING

A modification of our measurement protocol allows us to extract the mechanical dephasing time T_{2m} using coherent states of motion with varying amplitude. As shown in Fig. 3a, we now displace the mechanical state twice: once to initialize the measurement with a coherent state, and again after a variable delay τ . The two displacement pulses have identical amplitude and duration, but the second pulse has a programmed phase ϕ that is swept from 0 to 2π for each value of τ . The protocol concludes with a Ramsey measurement to characterize the final mechanical state.

We illustrate the principle behind this displacement interferometry protocol in Fig. 3b. The first displacement initializes a coherent state (Fig. 3b,i). After the second displacement, the resulting mechanical states lie on a circle in the complex plane. In the absence of dephasing ($\tau \ll T_{2m}$), maximal displacement 2α occurs at $\phi = 0$, and the final state is returned to the origin when the pulses are out of phase by $\phi = \pi$ (Fig. 3b,ii). In the presence of dephasing ($\tau \gtrsim T_{2m}$), this resulting path is shifted in the complex plane and no longer intersects the origin (Fig. 3b,iii). In these measurements, the final state size \bar{n} depends sinusoidally on ϕ , and the effect of dephasing can be seen in the reduced oscillation amplitude for larger delays (Fig. 3c). These amplitudes decay

exponentially in time at a rate $\gamma_{2m} = 1/T_{2m}$ (supplementary Section III). We fit the interference data to the following form to extract the amplitude C and offset \bar{n}_{off} :

$$\bar{n}(\phi) = C \cos(\phi + \phi_0) + \bar{n}_{\text{off}}. \quad (3)$$

The phase offset ϕ_0 is dependent on the delay τ , and could arise due to frequency uncertainty.

A few representative interferometry traces are shown in Fig. 3d for an initial state $\bar{n}_0 = 2.29$. Each interferogram is plotted relative to its offset \bar{n}_{off} for visual clarity. We note that the offsets also decay in time at a rate $\gamma_{1m} = 1/T_{1m}$, but the timescale of the interferometry data is insufficient to accurately determine this value. In Fig. 3e we plot the extracted offsets \bar{n}_{off} (inset), amplitudes C and exponential fit for this data set, from which we extract $T_{2m} = 2.2 \pm 0.2 \mu\text{s}$.

The effect of dephasing is also visible in the phonon number distribution of the mechanical oscillator. In principle, a coherent state undergoing amplitude decay should remain a coherent state and therefore maintain a Poisson distribution. However, in the presence of dephasing, the state evolves into something other than a coherent state whose $P(n)$ may deviate significantly from the Poissonian form. This effect is evident in Fig. 3f, where we examine $P(n)$ extracted from data for two representative states: one with $\tau = 0$ (top) and another with $\tau = 5.0 \mu\text{s}$ (bottom). Each distribution is compared to a coherent state $|\beta\rangle$ whose $P(n)$ is given by a Poisson distribution with the same average phonon number as the data, $|\beta|^2 = \bar{n}$. The top panel shows good agreement between the data (red bars) and the coherent state distribution (shaded blue), while the bottom panel shows a pronounced divergence between the two. We observe a similar effect in a simulation of the dephasing process (Fig. 4f).

We repeat the dephasing measurement for three distinct initial states and find, perhaps surprisingly, that the dephasing rate is reduced for larger phonon states. In a naive model, we expect the mechanical frequency jitter to be either primarily due to fluctuating off-resonant TLS, which would not be saturated by weakly driving the mechanics, or from excitation and relaxation of resonant TLS, which occur even when they are saturated. Saturation implies that the rates of phonon emission and absorption into the TLS bath are roughly equal, cancelling their effect on energy decay and leading to longer T_{1m} as we observe. However, dephasing should still occur if emission and absorption of phonons are occurring incoherently. An increase in T_{2m} may therefore point to coherence of the TLS bath with the driving field.

A NUMERICAL MODEL OF MECHANICS-TLS INTERACTION

To better understand these decay and decoherence signatures, we develop and study numerically [41] a highly simplified model of a mechanical mode interacting with

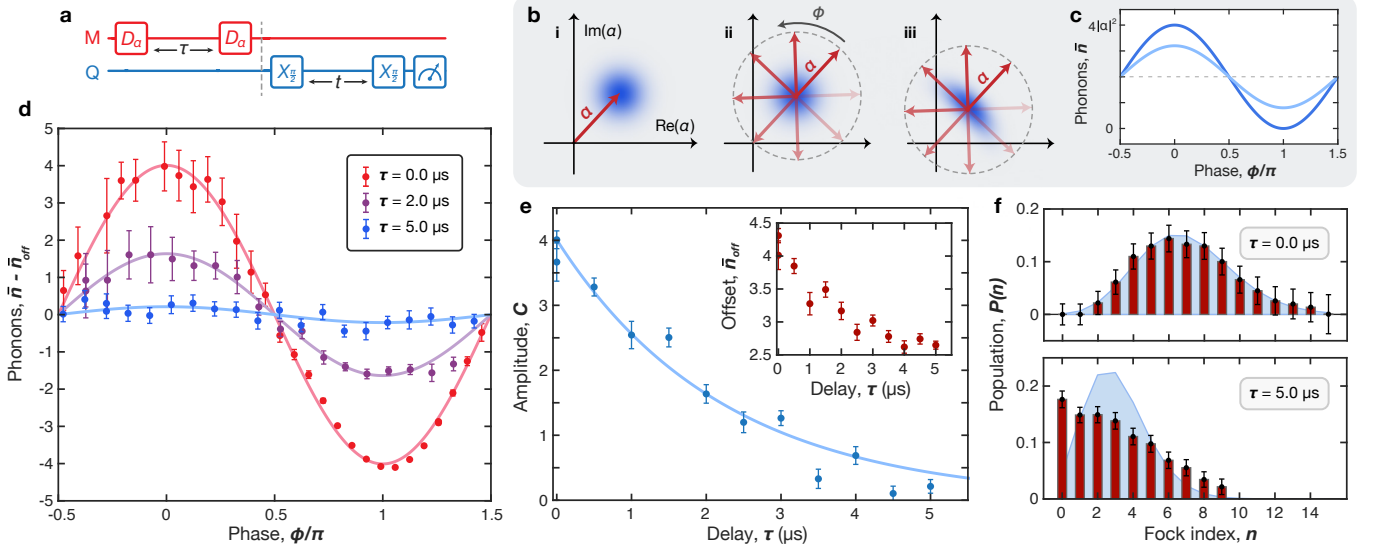


FIG. 3. **Displacement interferometry.** **a**, Pulse sequence for the dephasing measurement showing interferometry protocol (left) and mechanical state readout (right). We apply two displacement pulses \hat{D}_α separated by a variable delay τ and with a programmed relative phase ϕ . Last, we perform a Ramsey measurement to characterize the resulting mechanical state for each value of ϕ and τ . **b**, Illustration of the measurement principle. **i**, The initial displacement \hat{D}_α excites a coherent state. **ii**, The resulting states after the second displacement trace a circular path in phase space. In the absence of dephasing ($\tau \ll T_{2m}$), this path intersects the origin when $\phi = \pi$. **iii**, In the presence of dephasing ($\tau \gtrsim T_{2m}$), this circular path is shifted in phase space. **c**, Illustrated measurement result. For each value of τ , the average phonon number \bar{n} depends sinusoidally on ϕ . The case with no dephasing (**b,ii**) is plotted in dark blue, while the dephased case (**b,iii**) is shown in light blue. **d**, Experimental results. We plot the extracted phonon number (points) and corresponding fit to Eq. 3 (line) for a few values of τ with a common initial state size. **e**, Sample dephasing ringdown measurement. We plot the decaying amplitudes (points) extracted from the interference fringes and fit them to an exponential decay function (line) to extract the mechanical dephasing rate $\gamma_{2m} = 1/T_{2m}$. **f**, Dephasing effects in phonon distribution. Red bars indicate the Fock level occupations extracted from Ramsey data. Each panel corresponds to one data point \bar{n} in **d**. The shaded blue curve shows the $P(n)$ distribution of the coherent state with the same mean phonon number. The top panel ($\tau = 0$ and $\bar{n} = 6.97$) shows a mechanical state which closely follows a coherent state distribution, while the state in the bottom panel ($\tau = 5.0 \mu\text{s}$ and $\bar{n} = 3.06$) diverges notably from this distribution due to mechanical dephasing.

a small number of TLS [42]. Our model includes a collection of N identical two-level oscillators, with annihilation operators \hat{a}_k , coupled at a rate g_{TLS} to a harmonic oscillator (Fig. 4a). The TLS have intrinsic decay and dephasing rates γ_1 and γ_2 , respectively, and are detuned from the mechanical frequency by Δ_{TLS} . We assume there is no TLS-TLS coupling. In the frame of the TLS, the system Hamiltonian is given by:

$$\hat{H} = \Delta_{\text{TLS}} \hat{b}^\dagger \hat{b} + \sum_{k=1}^N g_{\text{TLS}} (\hat{a}_k^\dagger \hat{b} + \hat{b}^\dagger \hat{a}_k). \quad (4)$$

We initialize the mechanics and TLS in thermal states, each populated to a level $n_{\text{th}} = 0.05$. Next, we prepare the mechanical mode in a coherent state with an instantaneous displacement \hat{D}_α with variable amplitude. We then allow the system to freely evolve under the action of the Hamiltonian in Eq. 4 for a total duration of $50 \mu\text{s}$, with collapse operators acting on the TLS. The operators $\sqrt{\gamma_1(n_{\text{th}} + 1)}\hat{a}_k$ and $\sqrt{\gamma_1 n_{\text{th}}}\hat{a}_k^\dagger$ account for spontaneous emission and absorption in the TLS, while $\sqrt{\gamma_2/2}\hat{a}_k^\dagger \hat{a}_k$ accounts for their dephasing. Dissipation and decoherence of the phonon mode are induced by interactions with

the TLS; we do not include collapse operators for the mechanical mode itself.

The numerical solution to this Lindblad master equation returns the density matrix of the total system for every point in time. We examine the evolution of the mechanical mode's $P(n)$ and state size \bar{n} . Similar to experiment, the model shows approximately double-exponential energy decay in Fig. 4b, with weights and rates that depend on the initial state size. We fit each simulated decay profile to Eq. 2; to constrain the fit, we fix κ_1 to the mean of the experimentally observed values while allowing a_1 , a_2 and κ_2 to vary.

Although the measurements are insufficient to precisely determine the system parameters N , g_{TLS} , Δ_{TLS} , γ_1 and γ_2 , they provide guidance in our choice of values, and the resulting model helps to qualitatively understand the experimental data. It is possible to estimate the microscopic Hamiltonian parameters of the TLS from properties of the host material and the mechanical eigenmode (supplementary Section IV and Fig. S3). From the expected distribution of these parameters, the model produces reasonable agreement with experiments

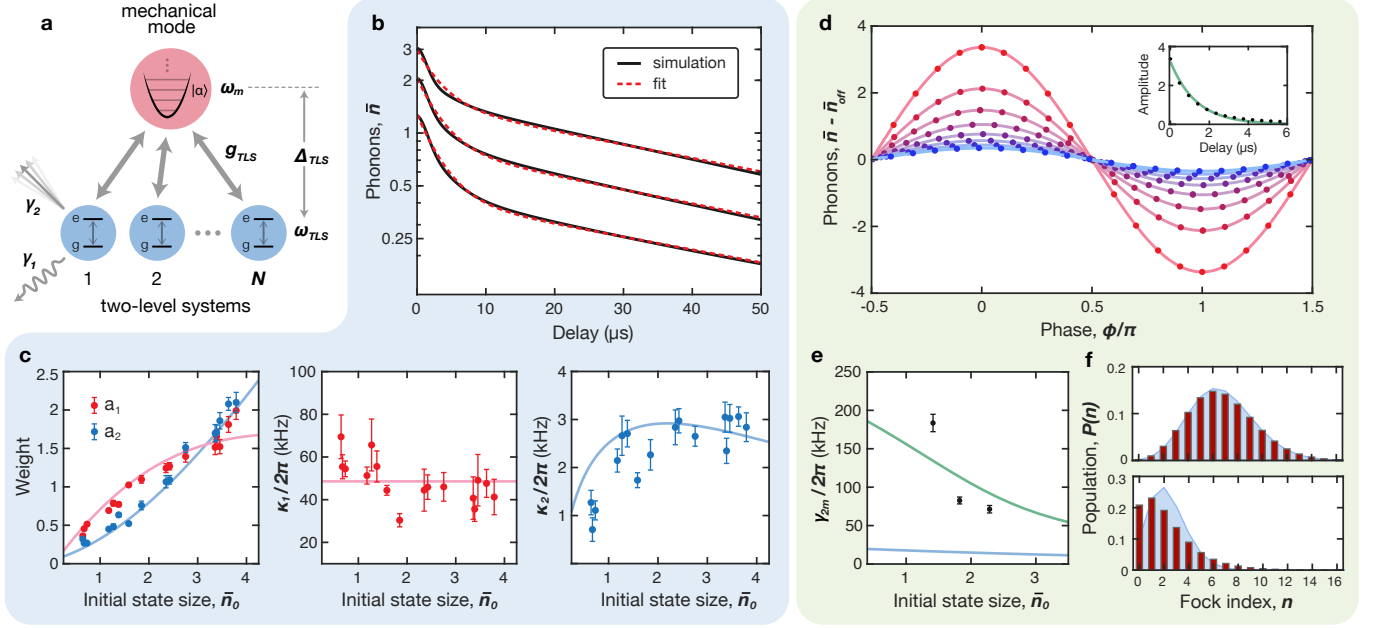


FIG. 4. **Modeling dissipation and decoherence.** **a**, Schematic of the simulation showing a collection of N two-level oscillators coupled at a rate g_{TLS} to the mechanical mode. The TLS are detuned from the mechanical mode by Δ_{TLS} and have an intrinsic decay rate γ_1 and dephasing rate γ_2 . **b**, Simulated mechanical state evolution showing TLS-induced dissipation for a range of initial state sizes. The mechanical energy decay, given by the average phonon number \bar{n} (black), follows a double-exponential trajectory, which we fit to Eq. 2 (red). **c**, Energy decay fit metrics from experimental data (points) and simulation (line) corresponding to the fast initial decay (red) and slow secondary decay (blue) are shown for a range of initial state sizes \bar{n}_0 . The left panel shows the exponential weights a_1 (red) and a_2 (blue). The middle panel shows the experimentally observed fast decay rates κ_1 (points) and their mean value (line). The right panel shows the fit results from experiment (points) and simulation (line) for the slow decay rate κ_2 . **d**, Representative result of the interferometry protocol for displacement amplitude $\alpha = 1.30$. The simulated phonon states (points) are fit to Eq. 3 (lines) for a range of delays in the time-evolved mechanical state. Inset shows the extracted amplitudes (points) and fit to exponential decay (line) from which we extract γ_{2m} . **e**, The experimentally observed dephasing rates (points) are compared to simulation results (lines) computed using two different coupling strengths g_{TLS} . The weak coupling limit ($g_{\text{TLS}}/2\pi = 33 \text{ kHz}$) corresponding to the results in b,c is shown in blue, while a larger coupling rate ($g_{\text{TLS}}/2\pi = 0.33 \text{ MHz}$) corresponding to d,f is shown in green. **f**, Effect of dephasing on $P(n)$. The simulated phonon distribution (red) is compared to the corresponding coherent state distribution (blue) at short delays (top, $\tau = 0$) and long delays (bottom, $\tau = 7.0 \mu\text{s}$).

for a range of values. In Fig. 4b,c we plot the results for $N = 5$, $g_{\text{TLS}}/2\pi = 33 \text{ kHz}$ and $\Delta_{\text{TLS}}/2\pi = 100 \text{ kHz}$. The lack of evidence of coherent mechanics-TLS energy exchange suggests that the TLS are rapidly dephasing, $\gamma_2/g_{\text{TLS}} \simeq 20 - 30$. For this simulation, we use $\gamma_2/2\pi = 660 \text{ kHz}$ and $\gamma_1/2\pi = 4.0 \text{ kHz}$. In Fig. 4b we plot the simulated energy decay trajectories (black) and corresponding fits (red) for a few initial states, and Fig. 4c shows good agreement between the fit metrics extracted from these simulations (lines) and the experimental data (points). See Fig. S3 for the corresponding TLS behavior.

To model the dephasing experiment, we apply a second displacement operation with phase $\phi \in [0, 2\pi]$ at a range of delays in the time-evolved mechanical state trajectory. Following the same procedure as before, we extract the sinusoidal amplitudes from the phonon interference fringes (Fig. 4d) and determine the TLS-induced γ_{2m} from the decaying amplitudes (Fig. 4d, inset). The results shown in Fig. 4d-f are computed with a stronger coupling rate ($g_{\text{TLS}}/2\pi = 0.33 \text{ MHz}$, $N = 5$, $\gamma_1/2\pi =$

4.0 kHz , $\gamma_2 = 20g_{\text{TLS}}$ and $\Delta_{\text{TLS}} = 3g_{\text{TLS}}$). In Fig. 4e, we compare the extracted γ_{2m} for these parameters to the experimental data, as well as to the weakly-coupled simulation results. For the weak-coupling parameters which match the energy decay experiments well, we find that the extracted γ_{2m} (blue line) is significantly lower than the experimentally observed values (points). With the stronger coupling rate, $g_{\text{TLS}}/2\pi = 0.33 \text{ MHz}$, the extracted γ_{2m} values (green line) fall within the range of our experimental observations. We note that for both values of g_{TLS} , the model predicts a reduced dephasing rate for larger phonon states. Finally, in Fig. 4f we show the simulated $P(n)$ for a short delay (top) and longer delay (bottom), where the dephasing effects can be seen as a deviation from the coherent state distribution.

The discrepancy in optimal simulation parameters suggests that our model provides an incomplete picture of the decoherence processes. For instance, it is possible that the mechanical mode suffers from additional dephasing channels, such as thermal excitation of low frequency

TLS. It is also possible that more complicated bath dynamics, such as a distribution of non-identical defects with TLS-TLS interactions, are necessary to more accurately describe our data.

CONCLUSIONS

In conclusion, we have applied a dispersive phonon number measurement to study coherent states in a phononic crystal resonator. We have examined how the energy decay and dephasing of these states depend on the initial phonon state size, and have reproduced some of these signatures using a simple model incorporating an ensemble of saturable TLS. Future studies would benefit from a more complex computational model, as well as additional measurements to probe the saturation dynamics, such as spectral hole burning [34]. Our results have direct relevance for bosonic error-correction schemes involving coherent states of phonons [2]. This measurement technique builds a foundation for further explorations of fundamental physics in quantum acoustic systems, including observing quantum jumps in mechanical states [43].

ACKNOWLEDGMENTS

The authors would like to thank M. I. Dykman and M. L. Roukes for useful discussions. The authors also thank R. G. Gruenke, K. K. S. Multani, N. R. Lee, T. Makihara, and O. Hitchcock. We acknowledge the support of the David and Lucille Packard Fellowship. This work was funded by the U.S. government through the Office of Naval Research (ONR) under grant No. N00014-20-1-2422, the U.S. Department of Energy through Grant No. DE-SC0019174, and the National Science Foundation CAREER award No. ECCS-1941826. A.Y.C. was

supported by the Army Research Office through the Quantum Computing Graduate Research Fellowship as well as the Stanford Graduate Fellowship. E.A.W. was supported by the Department of Defense through the National Defense & Engineering Graduate Fellowship. Device fabrication was performed at the Stanford Nano Shared Facilities (SNSF), supported by the National Science Foundation under grant No. ECCS-1542152, and the Stanford Nanofabrication Facility (SNF). The authors wish to thank NTT Research for their financial and technical support.

AUTHOR CONTRIBUTIONS

A.Y.C. and E.A.W. designed and fabricated the device and performed the experiments. A.Y.C. analyzed the data with E.A.W. assisting. A.Y.C. performed the simulations and wrote the manuscript with A.H.S.-N. assisting. A.H.S.-N. supervised all efforts.

ADDITIONAL INFORMATION

E. Alex Wollack is currently a research scientist at Amazon, and A. H. Safavi-Naeini is an Amazon Scholar. The other authors declare no competing financial interests. Correspondence and requests for materials should be addressed to A. H. Safavi-Naeini (safavi@stanford.edu).

DATA AVAILABILITY

The datasets generated and analysed for the current study are available from the corresponding author on reasonable request.

-
- [1] C. T. Hann, C.-L. Zou, Y. Zhang, Y. Chu, R. J. Schoelkopf, S. M. Girvin, and L. Jiang, *Phys. Rev. Lett.* **123**, 250501 (2019).
 - [2] C. Chamberland, K. Noh, P. Arrangoiz-Arriola, E. T. Campbell, C. T. Hann, J. Iverson, H. Putterman, T. C. Bohdanowicz, S. T. Flammia, A. Keller, G. Refael, J. Preskill, L. Jiang, A. H. Safavi-Naeini, O. Painter, and F. G. Brandão, *PRX Quantum* **3**, 010329 (2022).
 - [3] A. H. Safavi-Naeini and O. Painter, *New Journal of Physics* **13** (2011).
 - [4] A. Vainsencher, K. J. Satzinger, G. A. Peairs, and A. N. Cleland, *Applied Physics Letters* **109**, 033107 (2016).
 - [5] W. Jiang, C. J. Sarabalis, Y. D. Dahmani, R. N. Patel, F. M. Mayor, T. P. McKenna, R. Van Laer, and A. H. Safavi-Naeini, *Nature Communications* **11**, 1166 (2020).
 - [6] D. Mason, J. Chen, M. Rossi, Y. Tsaturyan, and A. Schliesser, *Nat. Phys.* **15**, 745 (2019).
 - [7] A. D. O’Connell, M. Hofheinz, M. Ansmann, R. C. Bialczak, M. Lenander, E. Lucero, M. Neeley, D. Sank, H. Wang, M. Weides, J. Wenner, J. M. Martinis, and A. N. Cleland, *Nature* **464**, 697 (2010).
 - [8] Y. Chu, P. Kharel, W. H. Renninger, L. D. Burkhardt, L. Frunzio, P. T. Rakich, and R. J. Schoelkopf, *Science* **358**, 199 (2017).
 - [9] Y. Chu, P. Kharel, T. Yoon, L. Frunzio, P. T. Rakich, and R. J. Schoelkopf, *Nature* **563**, 666 (2018).
 - [10] K. J. Satzinger, Y. P. Zhong, H.-S. Chang, G. A. Peairs, A. Bienfait, M.-H. Chou, A. Y. Cleland, C. R. Conner, É. Dumur, J. Grebel, I. Gutierrez, B. H. November, R. G. Povey, S. J. Whiteley, D. D. Awschalom, D. I. Schuster, and A. N. Cleland, *Nature* **563**, 661 (2018).
 - [11] P. Arrangoiz-Arriola, E. A. Wollack, Z. Wang, M. Pechal, W. Jiang, T. P. McKenna, J. D. Witmer, R. Van Laer, and A. H. Safavi-Naeini, *Nature* **571**, 537 (2019).
 - [12] L. R. Sletten, B. A. Moores, J. J. Viennot, and K. W. Lehnert, *Phys. Rev. X* **9**, 021056 (2019).
 - [13] A. Bienfait, K. J. Satzinger, Y. P. Zhong, H.-S. Chang, M.-H. Chou, C. R. Conner, É. Dumur, J. Grebel, G. A.

- Peairs, R. G. Povey, and A. N. Cleland, *Science* **364**, 368 (2019).
- [14] A. Bienfait, Y. Zhong, H.-S. Chang, M.-H. Chou, C. Conner, É. Dumur, J. Grebel, G. Peairs, R. Povey, K. Satzinger, and A. Cleland, *Phys. Rev. X* **10**, 021055 (2020).
- [15] Y. Chu and S. Gröblacher, *Applied Physics Letters* **117**, 150503 (2020).
- [16] E. A. Wollack, A. Y. Cleland, R. G. Gruenke, Z. Wang, P. Arrangoiz-Arriola, and A. H. Safavi-Naeini, *Nature* **604**, 463–467 (2022).
- [17] R. Manenti, M. J. Peterer, A. Nersisyan, E. B. Magnusson, A. Patterson, and P. J. Leek, *Phys. Rev. B* **93**, 041411 (2016).
- [18] G. S. MacCabe, H. Ren, J. Luo, J. D. Cohen, H. Zhou, A. Sipahigil, M. Mirhosseini, and O. Painter, *Science* **370**, 840 (2020).
- [19] E. A. Wollack, A. Y. Cleland, P. Arrangoiz-Arriola, T. P. McKenna, R. G. Gruenke, R. N. Patel, W. Jiang, C. J. Sarabalis, and A. H. Safavi-Naeini, *Applied Physics Letters* **118**, 123501 (2021).
- [20] J. Gao, M. Daal, J. M. Martinis, A. Vayonakis, J. Zmuidzinass, B. Sadoulet, B. A. Mazin, P. K. Day, and H. G. Leduc, *Applied Physics Letters* **92**, 212504 (2008).
- [21] N. Tubsrinuan, J. H. Cole, P. Delsing, and G. Andersson, *arXiv:2208.13410* (2022).
- [22] U. von Lupke, Y. Yang, M. Bild, L. Michaud, M. Fadel, and Y. Chu, *Nature Physics* **18**, 794 (2022).
- [23] D. Lachance-Quirion, S. Wolski, Y. Tabuchi, S. Kono, K. Usami, and Y. Nakamura, *Science* **367**, 425 (2020).
- [24] W. A. Phillips, *Rep. Prog. Phys.* **50**, 1657 (1987).
- [25] J. M. Martinis, K. B. Cooper, R. McDermott, M. Steffen, M. Ansmann, K. D. Osborn, K. Cicak, S. Oh, D. P. Pappas, R. W. Simmonds, and C. C. Yu, *Phys. Rev. Lett.* **95**, 210503 (2005).
- [26] C. Muller, J. H. Cole, and J. Lisenfeld, *Reports on Progress in Physics* **82**, 124501 (2019).
- [27] C. R. H. McRae, H. Wang, J. Gao, M. R. Vissers, T. Brecht, A. Dunsworth, D. P. Pappas, and J. Mutus, *Review of Scientific Instruments* **91**, 091101 (2020).
- [28] J. Gao, M. Daal, A. Vayonakis, S. Kumar, J. Zmuidzinass, B. Sadoulet, B. A. Mazin, P. K. Day, and H. G. Leduc, *Applied Physics Letters* **92**, 152505 (2008).
- [29] C. M. Quintana, A. Megrant, Z. Chen, A. Dunsworth, B. Chiaro, R. Barends, B. Campbell, Y. Chen, I. C. Hoi, E. Jeffrey, J. Kelly, J. Y. Mutus, P. J. J. O'Malley, C. Neill, P. Roushan, D. Sank, A. Vainsencher, J. Wenner, T. C. White, A. N. Cleland, and J. M. Martinis, *Applied Physics Letters* **105**, 062601 (2014).
- [30] P. V. Klimov, J. Kelly, Z. Chen, M. Neeley, A. Megrant, B. Burkett, R. Barends, K. Arya, B. Chiaro, Y. Chen, A. Dunsworth, A. Fowler, B. Foxen, C. Gidney, M. Giustina, R. Graff, T. Huang, E. Jeffrey, E. Lucero, J. Y. Mutus, O. Naaman, C. Neill, C. Quintana, P. Roushan, D. Sank, A. Vainsencher, J. Wenner, T. C. White, S. Boixo, R. Babbush, V. N. Smelyanskiy, H. Neven, and J. M. Martinis, *Phys. Rev. Lett.* **121**, 090502 (2018).
- [31] J. Lisenfeld, A. Bilmes, A. Megrant, R. Barends, J. Kelly, P. Klimov, G. Weiss, J. M. Martinis, and A. V. Ustinov, *npj Quantum Information* **5**, 105 (2019).
- [32] F. Hoehne, Y. A. Pashkin, O. Astafiev, L. Faoro, L. B. Ioffe, Y. Nakamura, and J. S. Tsai, *Phys. Rev. B* **81**, 184112 (2010).
- [33] J. Suh, A. J. Weinstein, and K. C. Schwab, *Applied Physics Letters* **103**, 052604 (2013).
- [34] G. Andersson, A. L. O. Bilobran, M. Scigliuzzo, M. M. de Lima, J. H. Cole, and P. Delsing, *npj Quantum Information* **7**, 15 (2021).
- [35] P. Arrangoiz-Arriola and A. H. Safavi-Naeini, *Phys. Rev. A* **94**, 063864 (2016).
- [36] J. Kelly, *Fault-tolerant superconducting qubits*, Thesis, University of California, Santa Barbara (2015).
- [37] K. J. Satzinger, C. R. Conner, A. Bienfait, H.-S. Chang, M.-H. Chou, A. Y. Cleland, É. Dumur, J. Grebel, G. A. Peairs, R. G. Povey, S. J. Whiteley, Y. P. Zhong, D. D. Awschalom, D. I. Schuster, and A. N. Cleland, *Appl. Phys. Lett.* **114**, 173501 (2019).
- [38] J. Koch, T. M. Yu, J. Gambetta, A. A. Houck, D. I. Schuster, J. Majer, A. Blais, M. H. Devoret, S. M. Girvin, and R. J. Schoelkopf, *Physical Review A* **76**, 042319 (2007).
- [39] S. Gustavsson, F. Yan, G. Catelani, J. Bylander, A. Kamal, J. Birenbaum, D. Hover, D. Rosenberg, G. Samach, A. P. Sears, S. J. Weber, J. L. Yoder, J. Clarke, A. J. Kerman, F. Yoshihara, Y. Nakamura, T. P. Orlando, and W. D. Oliver, *Science* **354**, 1573 (2016).
- [40] V. Singh, O. Shevchuk, Y. M. Blanter, and G. A. Steele, *Phys. Rev. B* **93**, 245407 (2016).
- [41] J. R. Johansson, P. D. Nation, and F. Nori, (2011), [10.1016/j.cpc.2012.02.021](https://arxiv.org/abs/10.1016/j.cpc.2012.02.021), [arXiv:1110.0573](https://arxiv.org/abs/1110.0573).
- [42] L. G. Remus, M. P. Blencowe, and Y. Tanaka, *Phys. Rev. B* **80**, 174103 (2009).
- [43] L. Sun, A. Petrenko, Z. Leghtas, B. Vlastakis, G. Kirchmair, K. M. Sliwa, A. Narla, M. Hatridge, S. Shankar, J. Blumoff, L. Frunzio, M. Mirrahimi, M. H. Devoret, and R. J. Schoelkopf, *Nature* **511**, 444 (2014).
- [44] J. Gao, *The Physics of Superconducting Microwave Resonators*, Thesis, California Institute of Technology (2008).
- [45] R. O. Behunin, F. Intravaia, and P. T. Rakich, *Phys. Rev. B* **93**, 224110 (2016).
- [46] J. Y. Duquesne and G. Bellessa, *Philosophical Magazine B* **52**, 821 (1985).

Supplementary information for “Studying phonon coherence with a quantum sensor”

I. MECHANICS DESIGN

To optimize the mechanical resonator design, we perform finite-element simulations using COMSOL Multiphysics, similar to those detailed in Ref. [11]. Our model includes a small sidewall angle $\theta_{\text{sw}} = 10^\circ$ and corners rounded with radius $r = 80 \text{ nm}$ to account for expected fabrication imperfections. We use X -cut, MgO-doped lithium niobate, with the crystal extraordinary axis oriented perpendicular to the cavity propagation axis. The frequency placement and bandwidth of the phononic bandgap depend on the geometry of the phononic crystal mirror cells. Our choice of design yields a simulated bandgap extending from approximately 1.9 to 2.5 GHz (Fig. S1a).

We also perform simulations of the mechanical cavity, which includes the defect site suspended by 4 mirror cells on each side. This is chosen for computational simplicity; the experimental device includes 8.5 mirror cells on each side. The resonant frequency of the localized mode is determined by the defect width, L_x . Target dimensions for both the defect and mirror cells are reported in Table S1. From the full structure simulations, we can extract the electromechanical admittance $Y(\omega)$ by simultaneously solving the electrostatic and elastic constitutive relations, coupled by the piezoelectric effect [35]. By applying an oscillating voltage boundary condition at the electrode surface and computing the induced current, we obtain the admittance as the ratio of the two. The simulated results are shown in Fig. S1d with a fit to an equivalent circuit model. From this fit, we extract the Butterworth-van Dyke circuit parameters $C_0 = 213.5 \text{ aF}$, $C_m = 51.4 \text{ aF}$, and $L_m = 90.9 \mu\text{H}$, corresponding to the equivalent circuit shown in the inset.

II. RAMSEY FIT FUNCTION

Though a decay rate proportional to phonon number is theoretically justified for linear decay of a bosonic mode, it is less suitable for our case, as coupling to TLS leads to more complex behavior. We attempted several approaches, including the original form from Ref. [16] as well as having independent κ_n for each Fock state. We found that for the types of phonon states being analyzed in this study, which have larger average phonon numbers than our previous work, a constant decay of κ assumed for all Fock states yields the best fit quality and stability. We roughly justify this by noting that since TLS are saturated by driving, larger Fock states will tend to have a relatively smaller decay than would be expected from a nonsaturable linear dissipation channel, and so a constant decay across all states is a useful heuristic for fitting the Ramsey signal. Importantly, we only assume this

state-independent decay to fit the 700 nanosecond duration of the Ramsey signal, t . The time-dependent phonon occupations are extracted from data over the longer period of measurement, τ .

III. COHERENT STATE DEPHASING

A harmonic oscillator with resonant frequency ω_0 and annihilation operator \hat{b} can undergo frequency fluctuations due to a stochastic process, $\eta(t)$, leading to a modulated resonant frequency $\omega(t) = \omega_0 + \eta(t)$. In the frame rotating at ω_0 , the quantum master equation which describes this process is given by:

$$\frac{d\rho}{dt} = \mathcal{D}\left[\frac{1}{\sqrt{T_{2m}}}\hat{b}^\dagger\hat{b}\right]\rho \quad (\text{S1})$$

where \mathcal{D} represents the Lindblad dissipator. Classically, these fluctuations of the harmonic oscillator's frequency lead to an equation of motion for a coherent state:

$$\frac{d\alpha}{dt} = -i\eta(t)\alpha \quad (\text{S2})$$

which, when integrated, leads to a coherent state amplitude $\alpha(t) = \alpha(0)e^{i\theta(t)}$ where $\theta(t) = \int_0^t \eta(t)dt$. This is reflected in the density matrix as

$$\rho(0) = |\alpha\rangle\langle\alpha| \rightarrow \rho(t) = \sum_{\theta} p(\theta) |\alpha e^{i\theta}\rangle\langle\alpha e^{i\theta}|. \quad (\text{S3})$$

The second displacement operation in the protocol of Fig. 3, with amplitude and phase $\alpha e^{i\phi}$, leads to:

$$D\rho(t)D^\dagger = \sum_{\theta} p(\theta) |\alpha e^{i\theta} + \alpha e^{i\phi}\rangle\langle\alpha e^{i\theta} + \alpha e^{i\phi}|. \quad (\text{S4})$$

The resulting phonon number in the oscillator is then given by

$$\begin{aligned} \langle n \rangle &= \sum_{\theta} p(\theta) |\alpha(e^{i\theta} + e^{i\phi})|^2 \\ &= |\alpha|^2 \sum_{\theta} p(\theta) (2 + e^{i\phi-i\theta} + e^{i\theta-i\phi}) \\ &= |\alpha|^2 (2 + e^{i\phi}\langle e^{-i\theta} \rangle + e^{-i\phi}\langle e^{i\theta} \rangle) \end{aligned} \quad (\text{S5})$$

The expectation values can be expanded as:

$$\langle e^{\pm i\theta} \rangle = \langle 1 \pm i\theta - \frac{\theta^2}{2} + \dots \rangle \quad (\text{S6})$$

For a stochastic process $\eta(t)$, the expected value for terms linear in θ are zero: $\langle \theta \rangle = \langle -\theta \rangle = 0$. For short times Δt , the quadratic terms are given by the correlation function $S_{\theta\theta}$:

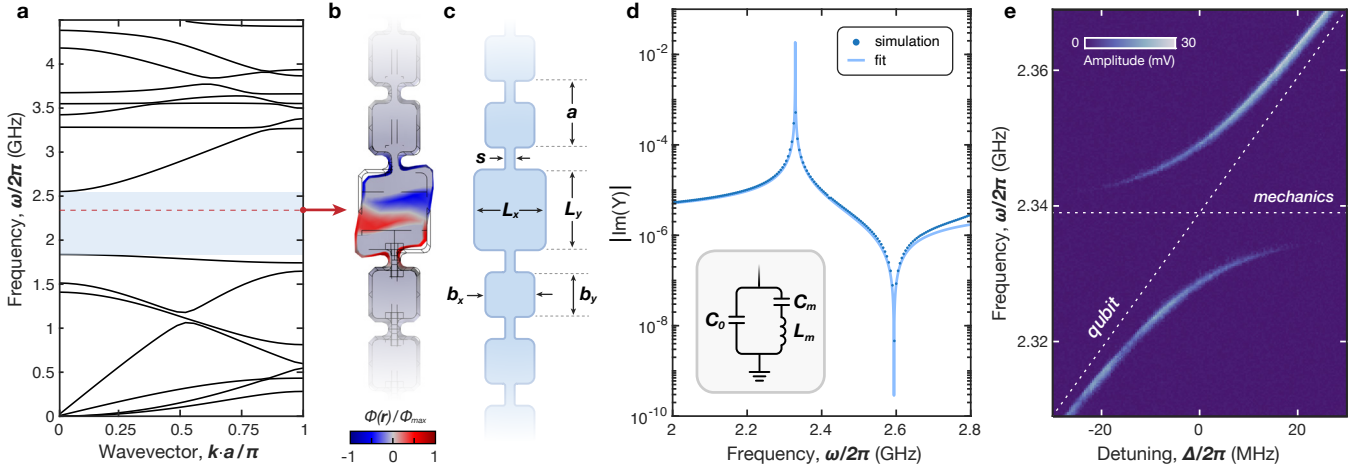


FIG. S1. **Phononic crystal cavity.** **a**, Simulated band structure for the phononic crystal mirror cells, with the primary bandgap highlighted in blue. The red dashed line indicates the measured mechanical frequency from our experimental device, $\omega_m/2\pi = 2.339$ GHz. **b**, Finite element simulation of the mechanical structure including mirror cells, defect site, and electrodes. The localized deformation of the eigenmode is visible, with the color plot indicating the electrostatic potential $\Phi(\vec{r})$. **c**, Important dimensions of the phononic crystal cavity, including both the mirror cells and defect site. Target values for these parameters are reported in Table S1. **d**, Simulated admittance $Y(\omega)$ near the mechanical resonance (points) and fit to an equivalent circuit model (line). Inset shows the Butterworth-van Dyke equivalent circuit. The circuit parameters C_0 , C_m and L_m extracted from the fit are reported in Sect. I. **e**, Measurement of the qubit excitation spectrum near the mechanical mode. Static flux-tuning of the qubit frequency modifies the detuning $\Delta = \omega_{ge} - \omega_m$ to show an avoided crossing between the two modes.

$$\langle \theta^2 \rangle = S_{\theta\theta}(\omega = 0)\Delta t = \frac{2\Delta t}{T_{2m}} \quad (S7)$$

More generally, $\langle \theta^n \rangle = 0$ for odd n , and $\langle \theta^{2n} \rangle \propto (\Delta t)^n$. This allows us to write Eq. S6 in terms of the time increment Δt and decoherence time T_{2m} :

$$\langle e^{\pm i\theta} \rangle = 1 - \frac{\Delta t}{T_{2m}} + \mathcal{O}(\Delta t)^2 = e^{-t/T_{2m}} \quad (S8)$$

Making this substitution in Eq. S5 brings us to the expected phonon number relation:

$$\langle n \rangle = 2|\alpha|^2(1 + e^{-t/T_{2m}} \cos \phi) \quad (S9)$$

IV. ESTIMATING MODEL PARAMETERS.

The interaction Hamiltonian describing a single TLS coupled to a strain field is given in Refs. [44, 45] as:

$$\hat{H}_{\text{int}} = \left(\frac{\Delta_{\text{as}}}{\varepsilon} \hat{\sigma}_z + \frac{\Delta_0}{\varepsilon} \hat{\sigma}_x \right) \gamma \cdot \xi \quad (S10)$$

Here, $\hat{\sigma}_x$ and $\hat{\sigma}_z$ are Pauli operators for the TLS, γ is the elastic dipole moment, and ξ is the strain field. Δ_0 and Δ_{as} represent, respectively, the tunneling energy and asymmetry energy from the bare TLS Hamiltonian, and $\varepsilon = \sqrt{\Delta_0^2 + \Delta_{\text{as}}^2}$ gives the associated eigenenergies, $\pm\varepsilon/2$. We can use this relation to estimate the

expected coupling rate between the TLS and the strain field, $g_{\text{TLS}} = \gamma \cdot \xi / \hbar$. The elastic dipole moment can be extracted from material constants and the measured loss tangent for our material platform:[26, 45]

$$\gamma = \sqrt{\delta_{\text{TLS}}^0 \frac{\rho v^2}{\pi P_0}}. \quad (S11)$$

Here v is the speed of sound in the host material, ρ the mass density, and P the spectral and spatial density of TLS states. For simplicity, we assume the longitudinal and transverse components of γ to be equivalent, and we use the RMS average of all strain components ξ_{ij} in our calculation.

From a finite-element simulation of the mechanical eigenmode, it is useful to calculate the effective mass

$$m_{\text{eff}} \equiv \frac{\int dV \rho |u(\vec{r})|^2}{\max |u(\vec{r})|^2} \quad (S12)$$

from which we can extract the displacement amplitude $x_{\text{zpf}} = \sqrt{\hbar/2m_{\text{eff}}\omega_m}$, which can be understood as the maximum zero-point fluctuation displacement. For the mode in question, we find $m_{\text{eff}} = 440$ fg and $x_{\text{zpf}} = 2.9$ fm. We can also calculate the average zero-point strain amplitude over the volume of the resonator

$$\bar{\xi}_{\text{zpf}} = \frac{x_{\text{zpf}}}{\max |u(\vec{r})|} \bar{\xi} \quad (S13)$$

where $\bar{\xi}$ represents the volume-averaged RMS value of all

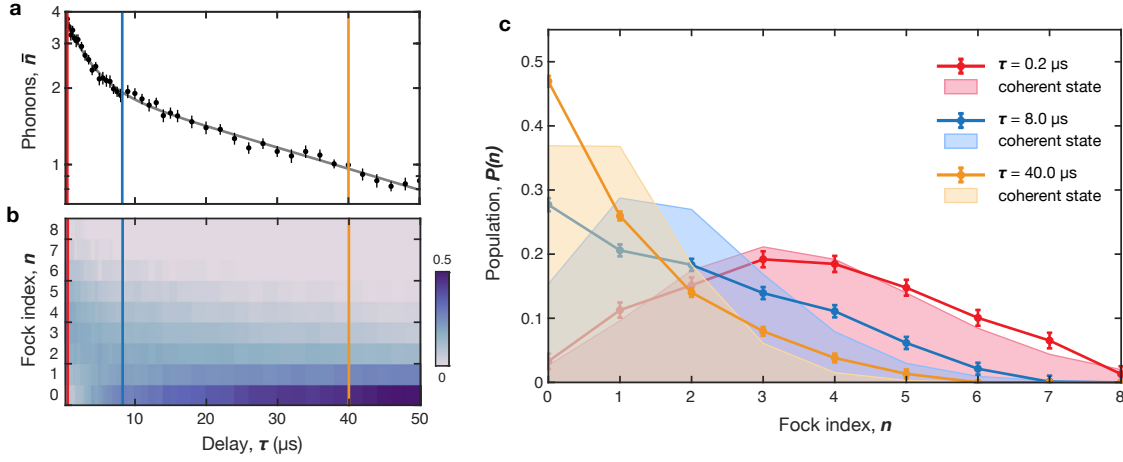


FIG. S2. **Phonon state evolution.** Here we show an expanded view of one ringdown measurement from Fig. 2 of the main text. **a**, Double-exponential ringdown trajectory showing data (points) and fit (line) and **b**, corresponding $P(n)$ evolution, reproduced from Fig. 2d,e. The color bar indicates the population $P(n)$ and vertical lines show the time slices selected for a closer examination. **c**, For each selected time slice, we compare the experimentally observed $P(n)$ (points and dark lines) to the coherent state distribution with the same average phonon number (shaded curves). Similar to the effect in Fig. 3f and Fig. 4f of the main text, we observe the measured state distributions diverge from the expected Poissonian form for longer delays.

strain components,

$$\bar{\xi} = \sqrt{\frac{1}{6V} \int dV (\xi_{xx}^2 + \xi_{xy}^2 + \xi_{xz}^2 + \xi_{yy}^2 + \xi_{yz}^2 + \xi_{zz}^2)}. \quad (\text{S14})$$

For the phononic crystal resonator mode, we find $\bar{\xi}_{\text{zpf}} = 1.6 \times 10^{-9}$.

The TLS-induced loss tangent at zero temperature δ_{TLS}^0 can be determined experimentally. Previous measurements of the temperature-dependent frequency shift of resonators with a similar geometry in this material platform provide an estimated value of the $F\delta_{\text{TLS}}^0$ product [19]. For our system, where we approximate that the TLS are distributed through the entire volume of the cavity, the filling factor is simply $F = 1$.

For the TLS density of states P_0 , we assume a value of order $10^{44} - 10^{46} \text{ 1/J}\cdot\text{m}^3$ based on literature values extracted for silica whose measured loss tangents are comparable to ours [24, 45]. We calculate the expected distributions for γ and g_{TLS} using Eq. S11 with randomly sampled P_0 and δ_{TLS}^0 . For each iteration, we randomly sample $P_0 = 10^{\lambda_1}$ with λ_1 uniformly distributed between [44, 46] and $\delta_{\text{TLS}}^0 = 10^{\lambda_2}$ with λ_2 uniformly distributed between $[-4.5, -4]$. We calculate these values using 10,000 iterations to compute the expected distribution for elastic dipole γ and coupling rate g_{TLS} , shown in Fig. S3d and S3e.

We can also use P_0 to estimate N , the number of TLS interacting with the mechanical mode. The relevant number to include in our numerical model is the number of TLS within the spatial volume of the resonator V and within a pertinent bandwidth $\delta\omega$ of the mechanical frequency. This bandwidth can be evaluated as $\delta\omega = \max(g_{\text{TLS}}, \gamma_2)$ where γ_2 is the decoherence

rate of the TLS. We must also consider the temperature-dependent distribution of the TLS, $P \neq P_0$. For the operating temperature of our experiment ($T = 10 \text{ mK}$), this is found to be $P \simeq 10P_0$ [46]. This allows us to extract

$$N = 10P_0 \times V \times \hbar\delta\omega \quad (\text{S15})$$

for a known P_0 and γ_2 . The calculations in existing TLS literature predict a much smaller γ_2 arising from TLS-TLS interactions [44]. Our simulation findings are not consistent with this prediction; the model reproduces our experimentally observed effects only in the limit of much faster γ_2 . For these values $\gamma_2/2\pi \gtrsim 500 \text{ kHz}$, Eq. S15 predicts $N \simeq 1 - 5$ TLS. Note that the faster than expected γ_2 is also consistent with the fact that we do not observe coherent oscillations between TLS and the mechanical resonance.

V. ERROR ANALYSIS.

We use Monte Carlo error propagation to determine the uncertainties for all values extrapolated from \bar{n} data. First, we extract $P(n)$ from the Ramsey signal $S(t)$ by nonlinear least squares regression, which returns an estimate for the $P(n)$ uncertainties from the fit parameters' covariance matrix. To determine the uncertainty on each calculated phonon number \bar{n} , we randomly resample $P(n)$ using the statistical uncertainty in each Fock level population to generate normally-distributed, zero-centered random noise. We repeat this process for 2,000 iterations and calculate \bar{n} at each iteration to build a distribution of values. The reported uncertainty represents the standard deviation of this distribution. The

Description	Parameter	Value
pitch	a	900 nm
strut width	s	70 nm
mirror cell width	b_x	575 nm
mirror cell length	b_y	625 nm
defect width	L_x	862 nm
defect length	L_y	1.0 μm
LN thickness		250 nm
Al electrode thickness		50 nm
mBVD coupling capacitance	C_0	213.5 aF
mBVD capacitance	C_m	51.4 aF
mBVD inductance	L_m	90.9 μH
LN mass density	ρ	4700 kg/m ³
acoustic wave velocity	v	4000 m/s
TLS density of states	P_0	$10^{45} - 10^{46}$ 1/J·m ³
loss tangent	δ_{TLS}^0	$10^{-4} - 10^{-4.5}$
effective mass	m_{eff}	440 fg
zero-point displacement	x_{zpf}	2.9 fm
zero-point RMS strain	$\bar{\xi}_{\text{zpf}}$	1.6×10^{-9}

TABLE S1. **Mechanical device parameters.** Physical dimensions, relevant material properties, and extracted parameters corresponding to the mechanical structure, host material, and eigenmode. Target dimensions for the phononic crystal mirror cells and defect site are indicated in Fig. S1. Some deviation from these values is expected in the experimental device due to fabrication disorder. Here, mBVD indicates equivalent circuit values from the modified Butterworth-van Dyke model.

same procedure is applied to determine the uncertainty in extracted values at each level of extrapolation; for fitted values, the resampled data are re-fit at each iteration. Fig. S4 shows the distributions generated by this procedure for fitted $T_{2\text{m}}$ in a displacement interferometry experiment as well as κ_1 and κ_2 from a representative nonlinear ringdown measurement.

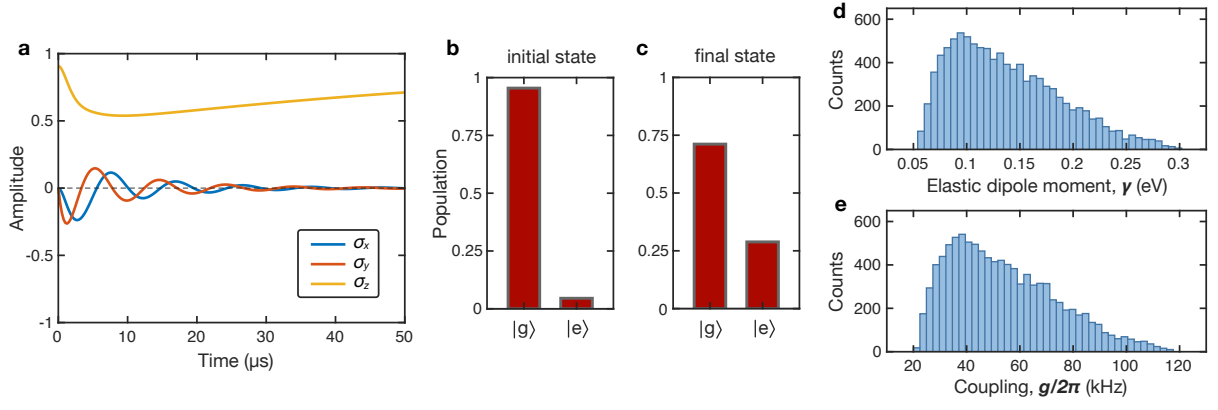


FIG. S3. **TLS state.** **a**, Simulated result showing all Bloch vector components of the TLS state for $g_{\text{TLS}}/2\pi = 32.8\text{ kHz}$, $N = 5$ and $\Delta_{\text{TLS}} = 3g_{\text{TLS}}$. **b**, Initial TLS state with a small thermal occupation in $|e\rangle$. **c**, Final TLS state at the end of the $50\text{ }\mu\text{s}$ simulation. **d**, Distribution of calculated elastic dipole moment γ and **e**, coupling rate g_{TLS} between the TLS and the strain field. Histograms are computed from 10,000 iterations of the calculation.

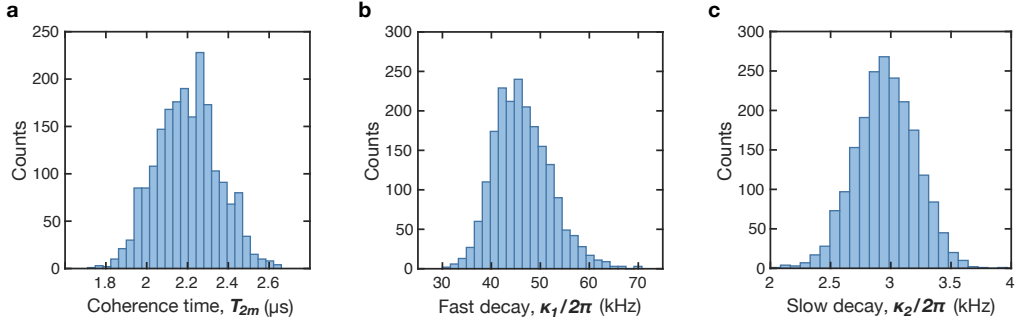


FIG. S4. **Results of uncertainty propagation.** **a**, Distribution of fitted T_{2m} values for initial state size $\bar{n}_0 = 2.29$. **b**, Fitted values for κ_1 and **c**, κ_2 for a common initial state size $\bar{n}_0 = 2.36$. All reported uncertainties represent the standard deviation of a distribution built from 2,000 repetitions.